RAA 2019 Vol. **19** No. **12**, 173(10pp) doi: 10.1088/1674–4527/19/12/173

http://www.raa-journal.org *http://iopscience.iop.org/raa*

Research in Astronomy and Astrophysics

Broken-up spectra of the loop-top hard X-ray source during a solar limb flare

Hao Ning[1], Yao Chen[1], Jeongwoo Lee[1], Zhao Wu[1], Yang Su[2] and Xiang-Liang Kong[1]

[1] Shandong Provincial Key Laboratory of Optical Astronomy and Solar-Terrestrial Environment, and Institute of Space Sciences, Shandong University, Weihai 264209, China; *yaochen@sdu.edu.cn*

[2] Purple Mountain Observatory, Chinese Academy of Sciences, Nanjing 210008, China

Received 2019 January 17; accepted 2019 June 3

Abstract Solar hard X-rays (HXRs) appear in the form of either footpoint sources or coronal sources. Each individual source provides its own critical information on acceleration of nonthermal electrons and plasma heating. Earlier studies found that the HXR emission in some events manifests a broken-up power-law spectrum, with the break energy around a few hundred keV based on spatially-integrated spectral analysis, and it does not distinguish the contributions from individual sources. In this paper, we report on the broken-up spectra of a coronal source studied using HXR data recorded by *Reuven Ramaty High Energy Solar Spectroscopic Imager* (*RHESSI*) during the SOL2017–09–10T16:06 (*GOES* class X8.2) flare. The flare occurred behind the western limb and its footpoint sources were mostly occulted by the disk. We could clearly identify such broken-up spectra pertaining solely to the coronal source during the flare peak time and after. Since a significant pileup effect on the *RHESSI* spectra is expected for this intense solar flare, we have selected the pileup correction factor, $p = 2$. In this case, we found the resulting *RHESSI* temperature ($\sim$30 MK) to be similar to the *GOES* soft X-ray temperature and break energies of 45–60 keV. Above the break energy, the spectrum hardens with time from spectral index of 3.4 to 2.7, and the difference in spectral indices below and above the break energy increases from 1.5 to 5 with time. However, we note that when $p = 2$ is assumed, a single power-law fitting is also possible with the *RHESSI* temperature higher than the *GOES* temperature by $\sim$10 MK. Possible scenarios for the broken-up spectra of the loop-top HXR source are briefly discussed.

Key words: acceleration of particles — Sun: corona — Sun: flares — Sun: UV radiation — Sun: X-rays — gamma rays

1 INTRODUCTION

In the standard picture of solar flares, called the CSHKP model (Carmichael 1964; Sturrock 1966; Hirayama 1974; Kopp & Pneuman 1976), energetic particles are accelerated through magnetic reconnection in the corona, some of them move downward along the field lines and then collide with the dense chromosphere to emit hard X-rays (HXRs) and γ-rays via a bremsstrahlung process. This produces intense footpoint HXR sources and heats the chromospheric plasmas to $\sim$10 MK. In a follow-up process, which is called chromospheric evaporation, the heated plasmas then move upward to fill in the post-flare loops to emit soft X-rays (SXRs).

In addition to the HXR footpoint sources and the SXR loop source, Masuda et al. (1994) found another HXR source located above the SXR loop, which is called the above-the-loop-top source or "Masuda-type" source. Similar sources have been observed in other events (e.g., Krucker et al. 2010; Oka et al. 2015; Chen et al. 2017), and they are considered as an important clue to particle acceleration in the corona.

A coronal HXR source is expected to be hardly visible because plasma is more dilute in the corona and bremsstrahlung emission there is weaker than in the footpoints. Also considering the limited dynamic range of present HXR imaging instruments, coronal sources are better observed in limb events with footpoint sources partially or fully occulted. Statistical surveys of limb flares found that coronal sources with significant non-thermal components form quite frequently (see, e.g., Krucker & Lin 2008; Effenberger et al. 2017). In some events, coronal sources are found to be associated with very-dense loop-tops and weak footpoint emission, and may emit in thick-target

bremsstrahlung (e.g., Sui et al. 2004; Veronig & Brown 2004).

The HXR spectra of solar flares usually appear in two components: thermal component at low energy range ($<$10–20 keV) and non-thermal component with a power law at higher energy range. In terms of temporal variation of HXR spectra, the majority of HXR spectra exhibits soft-hard-soft (SHS) evolution (e.g., Parks & Winckler 1969; Grigis & Benz 2004), while a small fraction of events manifests a soft-hard-harder (SHH) behavior (see, e.g., Frost & Dennis 1971; Cliver et al. 1986). These temporal variations have been used as constraints in modeling acceleration and transport of energetic electrons.

The properties of thermal components of HXR spectra vary in different events. Usually, the spectra contain a hot component with a temperature of $\sim$10 MK and high emission measure (EM). However, in some cases a so-called super-hot component has been reported (e.g., Caspi & Lin 2010; Caspi et al. 2014; Ning et al. 2018), with a temperature of over 30 MK, while the EM value is relatively lower. Plasmas with such high temperatures are believed to be a result of direct heating in the corona, rather than the chromospheric evaporation process.

In addition to the thermal/nonthermal components of solar HXR spectra, the nonthermal spectra may appear broken upward at high energies, namely spectral hardening at higher energies (e.g., Suri et al. 1975; Share et al. 2003; Shih et al. 2009; Ackermann et al. 2012). According to the statistical study by Kong et al. (2013), the break energy, E_b, is usually around a few hundred keV, and the difference in spectral indices below and above E_b ranges from 1.5 to 2.5.

Two scenarios have been proposed to explain the broken-up spectra. In one scenario, the broken-up spectra are attributed to the superposition of multiple sources with different spectral indices (Krucker et al. 2008). In the other scenario, it is attributed to the intrinsic property of the acceleration mechanisms, such as diffusive acceleration by the flare termination shock (Li et al. 2013) or the stochastic acceleration by wave-particle interactions (Hamilton & Petrosian 1992), which results in energetic electrons with a broken-up energy spectrum. It is also suggested that such broken-up spectra are due to the trap-and-precipitation of electrons within the loops (Park et al. 1997; Lee & Gary 2000; Minoshima et al. 2008).

To explore the origin of broken-up spectra of HXRs, it will be crucial to disentangle the contributions from spatially distinct sources because most previous studies are based on spatially-integrated HXR spectra. In this paper, we present our study of a spatially-resolved limb flare that exhibits a significant broken-up spectrum in the loop-top HXR source using imaging spectroscopy with the *Reuven Ramaty High Energy Solar Spectroscopic Imager* (*RHESSI*; Hurford et al. 2002; Lin et al. 2002). Section 2 presents the data and an overview of the event. Section 3 shows the analysis of *RHESSI* data of this event. The discussion and conclusions are presented in the last two sections respectively.

2 OBSERVATIONAL DATA AND EVENT OVERVIEW

We use the data from *RHESSI* and Atmospheric Imaging Assembly (AIA; Lemen et al. 2012) onboard the *Solar Dynamics Observatory* (*SDO*; Pesnell et al. 2012). *RHESSI* detects X-ray and γ-ray sources in the Sun with high cadence (4 s), and hight spatial ($3''$) and energy resolutions (as high as 1 keV). AIA has the capability of imaging plasma structures at temperatures from 20 000 K to over 20 MK, with high spatial ($0.6''$ pixel size) and temporal (12 s) resolutions in 10 different ultraviolet (UV) and extreme ultraviolet (EUV) passbands. AIA images at 171 ($\sim$0.6 MK) and 193 Å ($\sim$1.6 and 18 MK) are mainly used.

The *GOES* X8.2-class flare examined in this study occurred on 2017 September 10 from the active region (AR) 12673 at the western limb of the solar disk, accompanied by a fast coronal mass ejection (CME). There were four X-class flares and 27 M-class flares released from this AR (e.g., Yang et al. 2017; Sharykin & Kosovichev 2018). During the event considered in this study, part of the AR is on the back side of the solar disk, so that the flare footpoints are partially occulted. This yields a nice observation of both the morphology of the flaring structures with AIA and the coronal X-ray sources with *RHESSI*.

The X-ray lightcurves observed by *GOES*, *RHESSI* and *Fermi* Gamma-ray Burst Monitor (GBM, Meegan et al. 2009) are displayed in Figure 1(a), (b) and (c) respectively. *RHESSI* was in orbital nighttime until 15:52 UT, after which the X-ray flux at 3–300 keV rose sharply. From 15:52 UT to 15:54 UT, the attenuator state changed from A0 to A3 to cause large jumps in the X-ray flux, and the two abnormal peaks after 16:04 UT are also caused by the attenuator state change (from A3 to A1). We thus focus on the data from 15:54 UT to 16:04 UT. The X-ray flux of 100–300 keV rises to the peak at around 15:58 UT (t_1), and then decreases gradually.

At high energies (50–300 keV), we can see that the time profiles of the X-ray flux obtained by *Fermi* GBM are similar to those of *RHESSI*. Therefore, in this paper we focus on the analysis of *RHESSI* data. Note that the GBM data presented here are from the detector NAI_07, which is not the most sunward-facing one during this flare. This is to

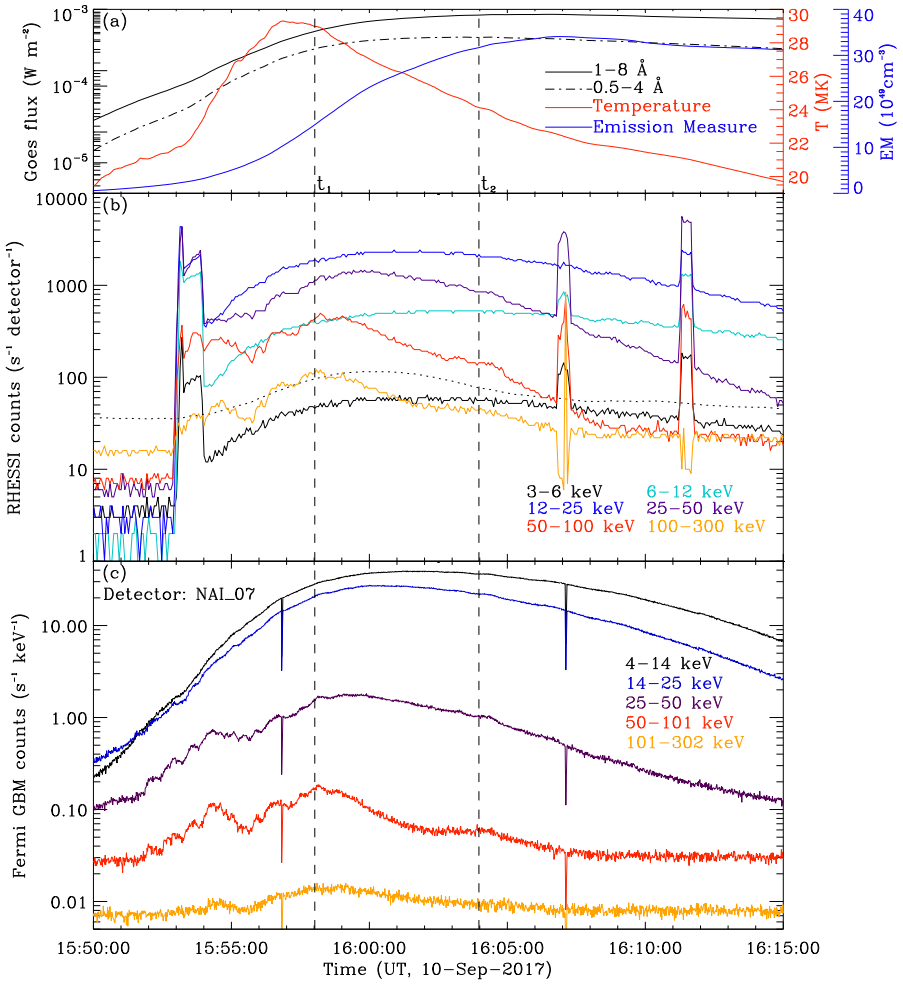

Fig. 1 Lightcurves of the 2017-Sep-10 flare observed by *GOES* (a), *RHESSI* (b) and *Fermi* GBM (c). The temporal profiles of the temperature (T) and EM derived from the *GOES* data are also shown in panel (a). In panel (b), the *dotted line* traces the temporal variation of the background of *RHESSI* data. The two *vertical dashed lines* mark the peak time of HXR (t_1, 15:58 UT) and SXR (t_2, 16:04 UT), respectively.

avoid the strong pileup and saturation issues since the flare is extremely intense. At lower energy, the flux peaks later (∼16:00 UT). The *GOES* SXR flux starts to increase earlier (∼15:50 UT) with a more gradual profile, and reaches its peak at 16:04 UT (t_2).

Figure 2 shows the EUV images observed by AIA. Initially, a bright bubble-like structure is observed at 171 and 193 Å, which ejects outward as the CME propagates at a speed of 400–600 km s^{-1}. During the process, the loop structures are stretched outward and re-close according to the data at 171 Å. A bright ray structure appears in 193 Å images. Other studies on this event suggest that the bubble represents a flux rope structure and the bright ray corresponds to the large-scale current sheet (see, e.g., Cheng et al. 2018). Other aspects that have been investigated are the complete eruptive process and characteristics of reconnection inflows (Yan et al. 2018), the association of the eruption of the bubble-like structure and flare energy release (Long et al. 2018), spatial distribution of high-energy electrons in a large region from the microwave perspective (Gary et al. 2018), and turbulent features within the ray-like structure (Cheng et al. 2018).

3 IMAGING AND SPECTRAL ANALYSIS OF *RHESSI* DATA

We focus on spectral characteristics of HXR emission from the loop top source during and after the peaking time of the X-ray flux. As Figure 2 exhibits, three time intervals are selected to represent the rising impulsive phase (panels (a)–(b)), the HXR peak (t_1, panels (c)–(d)) and the SXR peak (t_2, panels (e)–(f)). The sources are shown, superimposed onto the EUV images taken at nearby times.

At around 15:54 UT, the centroid of the 12–25 keV source is located in the corona, around 10″ above the limb, co-spatial with the loop-top observed at 171 Å. The source

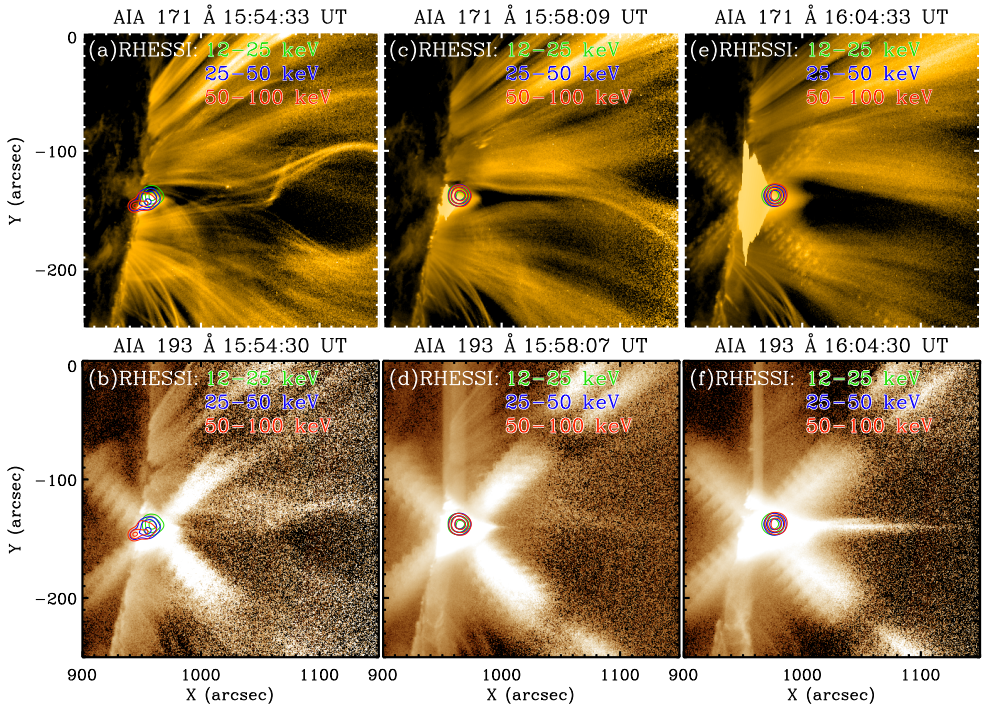

Fig. 2 EUV images of the event observed by *SDO*/AIA and *RHESSI* HXR sources. Panels (a), (c) and (e) are images at 171 Å, and panels (b), (d) and (f) show images at 193 Å. The contours represent the *RHESSI* sources at 12–25 keV (*green*), 25–50 keV (*blue*) and 50–100 keV (*red*). Contour levels are given by 30%, 60% and 90% of the maximal flux in each energy interval. The three moments of the EUV images correspond to the early stage of impulsive phase, the HXR peak time (t_1) and the SXR peak time (t_2), respectively. The HXR images are reconstructed by the CLEAN algorithm using detectors 3, 6 and 8. The time intervals for reconstructing the HXR sources are 15:54:15 UT–15:55:15 UT, 15:57:30 UT–15:58:58 UT and 16:04:00 UT–16:05:00 UT respectively.

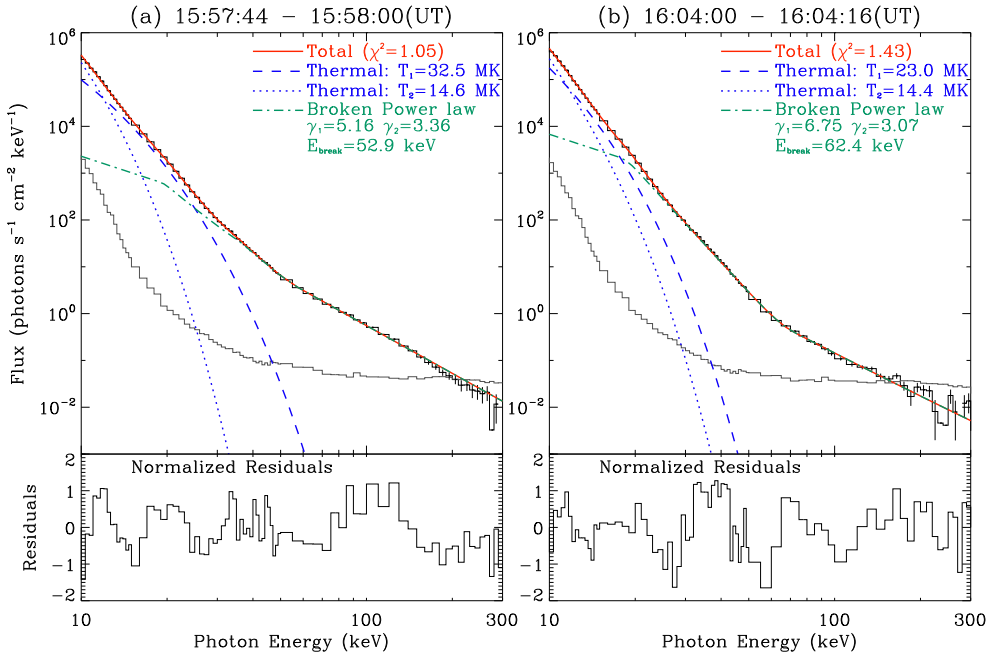

Fig. 3 Spectral analysis results of the spatially-integrated *RHESSI* flux spectra. (a) Spectrum at t_1. (b) Spectrum observed at t_2. The *histograms with black error bars* are the background-subtracted spectra, and the *red lines* represent the total fitting results. The background is given in *grey*. *Blue dotted lines* represent the hot components, and *blue dashed lines* represent super-hot components. Non-thermal components are given as *green lines*, representing broken power-law. The normalized residuals are shown as the histograms in the bottom-most panels. Data from detectors 1, 3, 6 and 8 are used.

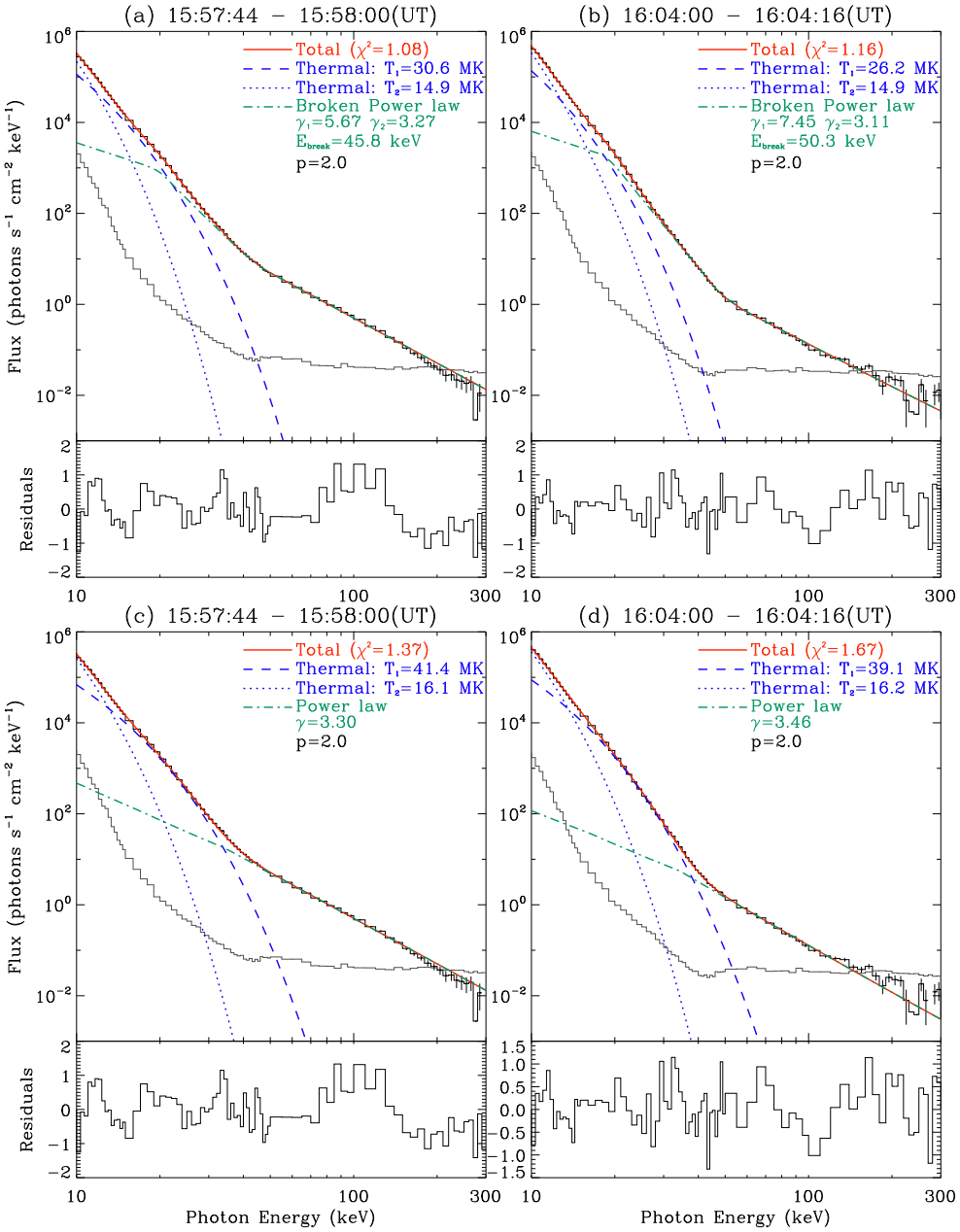

Fig. 4 Spectral fitting results with different models of the spatially-integrated *RHESSI* flux spectra. The detectors and the fitting components are the same as in Fig. 3. The coefficient of pileup effect (p) is set to be 2. In panels (a)–(b), the non-thermal part of the spectra is fitted with a broken power law, which is fitted with single power law in panels (c)–(d).

at 25–50 keV can be divided into two components with one coronal source and one footpoint source. The coronal component is slightly lower than the 12–25 keV loop-top source by about 4″–5″, while the footpoint component is relatively weak with an intensity of about 30% of the maximal flux. The 50–100 keV source also has one footpoint and one coronal component with the footpoint one being more intense.

At the HXR peak time (t_1), the centroids of different energy band sources are basically co-spatial with each other and located in the bright loop-top observed at EUVs around 15″ to 20″ above the disk. At the *GOES*-SXR peak time (t_2), the sources rise with the expansion of post-flare loops, and reach up to ∼30″ above the limb. All sources are very close to each other, yet there is a trend that the more energetic the source, the higher it is located.

The location of this HXR source above the limb has an advantage in that strong footpoint emissions are occulted, allowing us to focus on the spectral property of the loop-top source. A major difficulty, however, is the significant

pileup effect on the *RHESSI* spectra that is expected because this flare is so intense that it can acquire the *GOES* class X8.2. Therefore, we investigate the pileup effect in the spatially integrated *RHESSI* spectra, after which we proceed to study the temporal evolution and imaging spectroscopy.

3.1 Effect of Moderate Pileup on the HXR Spectra

We start the spectral fitting of the spatially-integrated *RHESSI* spectra with default parameters for the pileup correction[1]. Within Solar Software (SSW), this is the case when the pileup coefficient, p, is set to 1. The spectral fitting results around t_1 and t_2 are depicted in Figure 3. Panel (a) displays the spectra integrated from 15:57:44 UT to 15:58:00 UT, and panel (b) exhibits the spectra integrated from 16:04:00 UT to 16:04:16 UT. In this period, the footpoint source is not visible, and the loop-top source is dominant in the HXR emission.

The spectrum at t_1 can be fitted with two thermal components and a non-thermal component, and χ^2 is 1.05. Below 20–30 keV, the fit is given by a hot component with a temperature of 14.6 MK and a super-hot component with a temperature of 32.5 MK. We obtain the EM defined by EM $= n^2V$ where n is the plasma density and V is the source volume. The EMs of the two components are 2.9×10^{51} and 3.6×10^{49} cm^{-3}, respectively. The spectrum of the higher energy range can be fitted with a broken power-law distribution. The E_b is found to be 52.9 keV; the spectral index below E_b is $\gamma_1 = 5.16$ and the spectral index above E_b is $\gamma_2 = 3.36$. In summary, a significant broken-up feature of the spectra above E_b is observed, and the difference between the two spectral indices is $\Delta\gamma \equiv \gamma_1 - \gamma_2 = 1.8$.

Similarly, the *RHESSI* spectrum at t_2 (Fig. 3(b)) could also be fitted well by two thermal components (hot and super-hot) and one broken power-law component, with $\chi^2 = 1.43$. Due to the low photon count at high energies (above 200 keV), the fitting uncertainty is large there. We however focus on the spectra below 200 keV. In comparison with the spectrum at t_1, the broken-up feature of the spectrum at t_2 becomes more significant with $E_b = 62.4$ keV, $\gamma_1 = 6.75$ and $\gamma_2 = 3.07$. Thus, $\Delta\gamma = 3.68$, larger than that of t_1. In addition, the temperature of the hot component is 14.4 MK, and the temperature of the super-hot component is 23 MK. The EMs of the two components are 9.0×10^{51} and 1.6×10^{50} cm^{-3}, respectively. Comparing the fitting results, the temperature of the hot component around t_2 is close to that around t_1; the temperature of the super-hot components around t_2 is lower than that around t_1; and EM of both components around t_2 is higher than that around t_1. The changes of these parameters may indicate the cooling process associated with the super-hot component and the density increase in the post-impulsive stage of the flare.

3.2 Effect of Strong Pileup on the HXR Spectra

At the time of the event, the *RHESSI* detectors suffered from accumulated radiation damage after long-term operation. This may make the pileup effect more significant, particularly when observing extreme events such as the present one. We thus test the possible extent of the pileup effect, by adopting larger values of $p > 1$.

In Figure 4(a)–(b) we plot the fitting results of spatially-integrated spectra at t_1 and t_2, with $p = 2$. The same models including two thermal components and one broken power-law component are used. We obtained (a) $E_b = 45.8$ keV, $\gamma_1 = 5.67$ and $\gamma_2 = 3.27$ with $\chi^2 = 1.08$ at t_1, and (b) $E_b = 50.3$ keV, $\gamma_1 = 7.45$ and $\gamma_2 = 3.11$ with $\chi^2 = 1.16$ at t_2. The temperatures of the two thermal components are 14.9 and 30.6 MK at t_1, while 14.9 and 26.2 MK at t_2. Comparing with the default case (Fig. 3), we found that the temperature and spectral indices do not change much, but the break energy is lower, for both t_1 and t_2. In panels (c)–(d) of Figure 4, we attempt alternative models consisting of two thermal components plus one single power-law component, which become plausible when a larger p is adopted. This does not result in much change in the power-law index, γ_2. However, the temperature increases to $\sim$16 MK and 39–41 MK for the two thermal components, and χ^2 also increases to 1.37 and 1.67, as compared to the default case (Fig. 3).

As displayed in Figure 1(a), the *GOES* data provide temperature around 29 MK at t_1 and 24 MK at t_2. This is consistent with the temperature, T_1, found for the double power-law spectrum. On the other hand, the single power-law spectrum, which is found to be feasible with a higher p, predicts much hotter thermal components reaching $\sim$40 MK. As a comparison, we note that earlier studies also present a super-hot component with such high temperature, and it was indicated that the *RHESSI* temperature can be higher than the *GOES* temperature (e.g., Holman et al. 2003; Caspi & Lin 2010; Caspi et al. 2014; Warmuth & Mann 2016). Therefore, the single power-law interpretation cannot be completely ruled out for this flare, considering the significant pileup effect on spectral fitting.

We also tested the spectral fitting with $p = 3$, in which case lower temperatures and harder nonthermal electrons are required, as well as high values of EM (EM $\sim$ 10^{54} cm^{-3}). Since this is much higher than the EM ob-

[1] Two photons close in time are detected as one photon and have their energies added. A pileup of three or more photons is possible, but at a much lower probability (Smith et al. 2002).

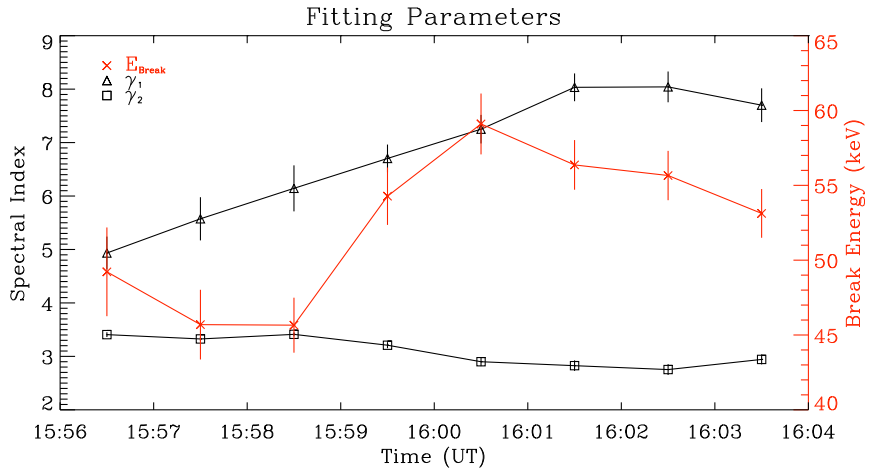

Fig. 5 Temporal variation of the spectral fit parameters with error bars. Total spectra in eight time intervals from 15:56 UT to 16:04 UT are fitted with two thermal and one broken power-law component, while p is set to be 2. Symbols represent γ_1 (*triangles*), γ_2 (*squares*) and E_b (*crosses*).

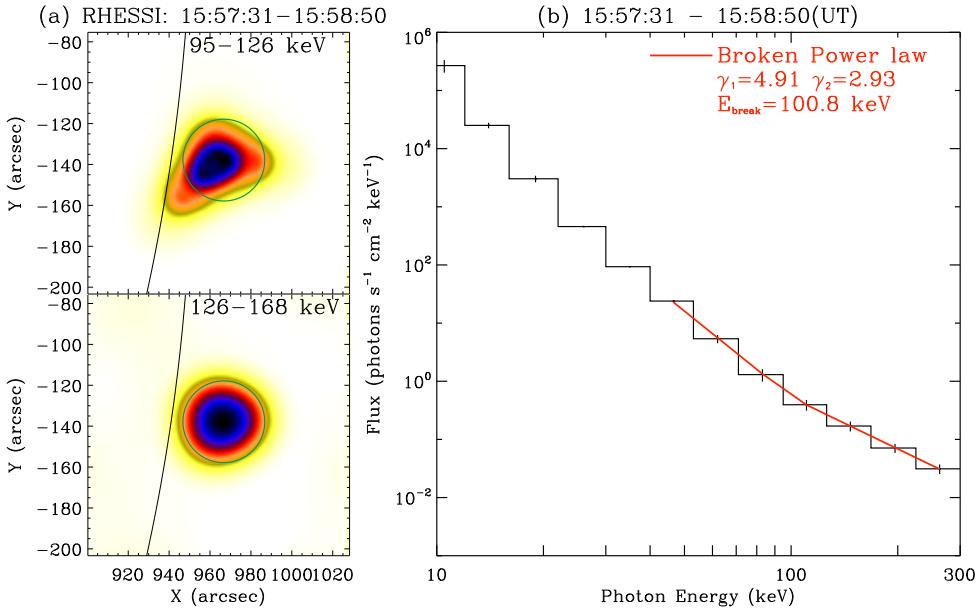

Fig. 6 Imaging spectroscopic results at t_1. (a) Images reconstructed in the two energy bands. *Green circles* represent the region that we utilized for determining the spectra. (b) The obtained imaging spectrum. The local spectrum constructed from the maps is plotted in histogram mode with error bars. The *red line* represents the broken power-law of 40–300 keV, to fit the non-thermal part of the spectra. The PIXON algorithm along with the data from detectors 6 and 8 are used to reconstruct these images.

tained with $p = 1$ or 2 (EM $\sim 10^{51}$ cm^{-3}), we consider it unrealistic. When we enforce a single power-law solution to the spectrum with $p = 1$, χ^2 comes out too high ($\sim$ 3–5) and the temperature becomes unrealistically high (over 60 MK). We therefore found the fairly good single power-solution with the pile-up correction around $p = 2$.

3.3 Temporal Evolution

We proceed to investigate the temporal evolution of the HXR spectrum with $p = 2$. We divide the period from 15:56 UT to 16:04 UT into eight intervals with 1-min duration each. We fit the spectrum within each time interval using the above method with two thermal components and one broken power-law component, and found χ^2 around 1 in all cases. The derived temporal profiles of three fitting parameters (E_b, γ_1 and γ_2) are shown in Figure 5.

From 15:57 UT to 16:01 UT, E_b increases from 45 to 59 keV, and then declines to around 55 keV from 16:01 UT to 16:04 UT. During the 8 min, γ_1 increases from 5 to 8, and γ_2 decreases slightly from 3.4 to 2.7, and $\Delta\gamma$ increases

continuously from ∼1.5 to 5. This indicates that the spectrum below E_b becomes softer and the spectrum above E_b becomes harder, i.e., the broken-up feature becomes more and more significant with time, during the impulsive phase to the decay phase.

3.4 Imaging Spectroscopy

The spectra analyzed above are spatially integrated over the full disk (hereafter called the total spectra). As mentioned, the footpoint source is not visible after 15:56 UT, therefore, the X-ray spectra analyzed above are unambiguously associated with the loop-top source. To confirm this (and relevant results) using spatially-resolved data, we obtain imaging spectra around t_1 (from 15:57:31 UT to 15:58:50 UT) using the SSW OSPEX package. This is done by first reconstructing the HXR sources for different energy bands, and then integrating the photon flux within specified area for each energy band.

The loop-top source in the two energy bands (95–126 keV and 126–168 keV) is displayed in Figure 6(a), from which we calculate the total counts of photon within the green circle for each energy band. The resulting spatially-resolved spectrum is depicted as a histogram in Figure 6(b). The spectrum can be fitted again using two thermal components and one broken-power-law component. Because the energy range is coarse and the pileup effect cannot be corrected, we did not show the total fitting result, but only the non-thermal part (over 40 keV). In this part, the broken-up feature is noticeable, as expected. We found the break energy, $E_b = 100.8$ keV, higher than that obtained with the spatially-integrated spectra, and the indices $\gamma_1 = 4.91$ and $\gamma_2 = 2.93$ with $\Delta\gamma = 1.98$.

The differences between the spatially-integrated spectroscopy-only result and the result of the imaging spectroscopy are not significant, but may need explanation. We corrected the pile-up effect of *RHESSI* data for the total spectral analysis, but not for the imaging spectroscopic analysis. We also note that wider energy bands are utilized for the imaging spectroscopy than those for the total spectral analysis in order to have sufficient number of photons. These could have resulted in the different spectral indices and break energy obtained with the two methods.

4 DISCUSSION

4.1 Nature of the HXR Loop-top Source

In the present event, one footpoint source appears only at the start of the impulsive phase in high-energy passbands (25–100 keV). During the flare peak time and after, the loop-top source is the only HXR source and does not show any significant extension toward the footpoints. It is possible that the footpoint source becomes occulted by the disk due to solar rotation or simply the footpoint source diminishes with time.

Here we elaborate another possibility that in the loop-top filled up with dense plasma due to chromospheric evaporation, electrons lose most of their energy via thick-target bremsstrahlung and as a result, not many energetic electrons reach the chromosphere to produce strong footpoint HXR. We calculate the minimum energy, $E_{\rm min}$, of electrons that can reach the footpoint against Coulomb collisions using the *RHESSI* data and geometry of the flaring loop. At t_1, the EM of the hot component derived from *RHESSI* data is EM $\approx 2.9 \times 10^{51}$ cm^{-3}; the HXR source size is $R \approx 15''$ (determined with the 10% contour of the 25–50 keV source at t_1) and the distance from the loop-top to the footpoint is estimated as $L \approx 30''$. We thus estimate the density in the loop-top as $n \equiv (3{\rm EM}/4\pi R^3)^{1/2} \approx 8.0 \times 10^{11}$ cm^{-3}, and the corresponding column depth is $nL \approx 1.6 \times 10^{21}$ cm^{-2}. Thus, under Coulomb collisions, the electrons with energies lower than $E_{\rm min} \approx (8.8\,{\rm keV})(nL/10^{19}{\rm cm}^{-2})^{1/2} \approx 110$ keV cannot reach the footpoint (Brown 1973). More energetic electrons with ≥110 keV can reach the footpoint, but are insufficient in number to produce significant HXR. This supports our thick-target interpretation of the coronal loop-top source and is also consistent with some earlier results (see, e.g., Sui et al. 2004; Veronig & Brown 2004; Jiang et al. 2006).

4.2 Origin of the Broken-up Spectra

There are two main scenarios for the HXR broken-up spectra: they were either emitted by two groups of electrons with different power-law indices or from a single group of electrons evolving into a broken power-law distribution in energy (see Sect. 1).

The first scenario has been proposed by Krucker et al. (2008) to explain the broken-up feature of the total spectra observed for three events, for which they found that the spectra of loop-top sources are harder than the spectra of footpoint sources and that the total spectrum manifests hardening. We note that this scenario is consistent with earlier simulations of stochastic acceleration of solar flare electrons by Park et al. (1997). In their simulation, the total X-ray emission is regarded as a superposition of thin-target emission of trapped electrons in the loop-top and thick-target emission of precipitating electrons into the footpoint, which explains two flares from the GRS instrument in 1989 and two from the EGRET and BATSE instruments in 1991. Li & Gan (2011) also proposed that the broken-up spectrum can be produced either by the summa-

tion of individual sources or by the temporal variation of a single source. However, we note that the present broken-up spectra observed by *RHESSI* pertain to the loop-top source only, and therefore does not fit into this scenario.

In the second scenario, the broken-up photon spectrum is due to physical characteristics of a certain acceleration mechanism and/or a transport process of electrons. We consider two acceleration models as more relevant to our observation. The first is the model of diffusive shock acceleration at the flare termination shock developed by Li et al. (2013). They suggested that electrons with a few hundred keV can further resonate with MHD turbulence in the inertial range to achieve additional acceleration. This results in a hardening spectrum around 500–600 keV, and the power-law indices of the electron energy distribution below and above the break energy are $\alpha_{1,2} \approx 10$ and 5, respectively. After converting the model electron energy distribution to photon spectrum under the thick-target approximation of bremsstrahlung (White et al. 2011), we find $\gamma_1 \approx 8.5$, $\gamma_2 \approx 3.5$, comparable with our fitting results at t_2. However, the break energy in their model amounts to 200–300 keV in the photon spectrum, which is much higher than our results. In their model, the break energy is associated with the spatial scale separating the inertial range and the dissipation range of turbulence, which could be either Larmor radius or inertial length of ions. Therefore, predicted break energy varies with plasma temperature, density and magnetic field. For typical coronal values of these parameters, the model predicts a break energy much higher than what is derived from our data analysis, with a rough estimate (which is not shown here).

The second model includes stochastic acceleration via wave-particle interactions in the presence of Coulomb collisions. As presented in Hamilton & Petrosian (1992), Coulomb collisions are more effective at energies below a certain energy threshold, E_c, where acceleration by waves is balanced by Coulomb collisional energy loss. Thus, electron distribution below E_c becomes quasi-thermal, and that above E_c is non-thermal and harder. According to their results, the spectra show gradual steepening at low energies (< 30 keV) together with decreasing E_c (equivalent to E_b in our study), as density of ambient plasma increases.

Finally, we consider a third scenario that is related to the so-called trap-and-precipitation model, in which Fokker-Planck solutions for electrons in a magnetic trap are used to demonstrate the hardening of electron energy distribution in the trap (Lee & Gary 2000; Minoshima et al. 2008). In this model, the hardening occurs because lower-energy electrons either lose energy or escape from the trap more rapidly under Coulomb collisions while higher-energy electrons can survive longer in the trap. This model describes the transport effect with acceleration mechanisms unspecified. Other than that, the same physics is already included in Hamilton & Petrosian (1992).

5 CONCLUSIONS

We have presented a spectral analysis of a strong loop-top HXR source during the SOL2017-09-10T16:06 flare, for which a main issue was the pileup effect on the *RHESSI* spectra. After several tests of the *RHESSI* spectral fittings, we chose a pileup correction as high as $p = 2$ to accommodate the strong pileup effect in this event. It follows that the loop-top source during and after the HXR maximum phase consists of a broken-up power law spectrum from $\gamma = 5.7$ to 3.3. The break energy of the spectrum is around $E_b \approx 46$–50 keV, which tends to be lower than those reported in previous studies. The spectrum above E_b becomes harder with time, and the difference in indices below and above E_b increases from 1.5 to 5. It is suggested that the loop-top source may work as a thick-target to the bremsstrahlung emission due to the dense plasma in the loop-top, and that the broken-up spectrum is due to the corresponding hardening of electron energy distribution while trapped in the loop-top.

We tentatively suggest that either the diffusive shock (or stochastic acceleration) or the transport effects under Coulomb collisions should be more relevant to the present observation, rather than the superposition of different sources. However, further studies are needed to figure out which of the above processes is more dominant or if a combination of multiple processes is responsible for the detailed behavior of the HXR spectrum derived in this study. This study also indicates that a combination of a single power-law nonthermal component and a super-hot component cannot be ruled out when a strong pileup effect as high as $p = 2$ is assumed. To confirm the possibility of the double power-law spectrum in similar events, more advanced X-ray instruments of solar flares such as that aboard the *Advanced Space-based Solar Observatory* (*ASO-S*; Gan et al. 2015), the Spectrometer Telescope for Imaging X-rays (STIX; Krucker et al. 2016) onboard the *Solar Orbiter* (Müller et al. 2013) and the *Focusing Optics X-ray Solar Imager* (*FOXSI*; Christe et al. 2017) with more events and data with higher quality will be needed to confirm the broken-up HXR spectra in the loop-top source.

Acknowledgements The authors thank the *RHESSI* and *SDO* teams for the high-quality X-ray and EUV data. We thank Prof. Vahé Petrosian for constructive comments on the stochastic acceleration model. We also thank Dr. Baolin Tan for helpful discussion. This work was supported by the National Natural Science Foundation of

China (NSFC, Grant Nos. 11790303 41774180, 11703017 and 11873036). X.K. also acknowledges support from the Young Elite Scientists Sponsorship Program by the China Association for Science and Technology, and the Young Scholars Program of Shandong University, Weihai. Y.S. acknowledges the Joint Research Fund in Astronomy (U1631242 and U1731241) under the cooperative agreement between NSFC and CAS, the Major International Joint Research Project (11820101002) of NSFC and the "Thousand Young Talents Plan".

References

Ackermann, M., Ajello, M., Allafort, A., et al. 2012, ApJ, 745, 144
Brown, J. C. 1973, Sol. Phys., 31, 143
Carmichael, H. 1964, Proc. of the AAS-NASA Symp., 50, 451
Caspi, A., Krucker, S., & Lin, R. P. 2014, ApJ, 781, 43
Caspi, A., & Lin, R. P. 2010, ApJ, 725, L161
Chen, Y., Wu, Z., Liu, W., et al. 2017, ApJ, 843, 8
Cheng, X., Li, Y., Wan, L. F., et al. 2018, ApJ, 866, 64
Christe, S., Shih, A. Y., Krucker, S., et al. 2017, AGU Fall Meeting Abstracts, 2017, SH44A-07
Cliver, E. W., Dennis, B. R., Kiplinger, A. L., et al. 1986, ApJ, 305, 920
Effenberger, F., Rubio da Costa, F., Oka, M., et al. 2017, ApJ, 835, 124
Frost, K. J., & Dennis, B. R. 1971, ApJ, 165, 655
Gan, W., Deng, Y., Li, H., et al. 2015, SPIE, 9604, 96040T
Gary, D. E., Chen, B., Dennis, B. R., et al. 2018, ApJ, 863, 83
Grigis, P. C., & Benz, A. O. 2004, A&A, 426, 1093
Hamilton, R. J., & Petrosian, V. 1992, ApJ, 398, 350
Hirayama, T. 1974, Sol. Phys., 34, 323
Holman, G. D., Sui, L., Schwartz, R. A., & Emslie, A. G. 2003, ApJ, 595, L97
Hurford, G. J., Schmahl, E. J., Schwartz, R. A., et al. 2002, Sol. Phys., 210, 61
Jiang, Y. W., Liu, S., Liu, W., & Petrosian, V. 2006, ApJ, 638, 1140
Kong, X., Li, G., & Chen, Y. 2013, ApJ, 774, 140
Kopp, R. A., & Pneuman, G. W. 1976, Sol. Phys., 50, 85
Krucker, S., Hudson, H. S., Glesener, L., et al. 2010, ApJ, 714, 1108
Krucker, S., Hurford, G. J., MacKinnon, A. L., Shih, A. Y., & Lin, R. P. 2008, ApJ, 678, L63
Krucker, S., & Lin, R. P. 2008, ApJ, 673, 1181
Krucker, S., Bednarzik, M., Grimm, O., et al. 2016, Nuclear Instruments and Methods in Physics Research Section A: Accelerators, Spectrometers, Detectors and Associated Equipment, 824, 626, Frontier Detectors for Frontier Physics: Proceedings of the 13th Pisa Meeting on Advanced Detectors, *https://ui.adsabs.harvard.edu/abs/2016NIMPA.824..626K*
Lee, J., & Gary, D. E. 2000, ApJ, 543, 457
Lemen, J. R., Title, A. M., Akin, D. J., et al. 2012, Sol. Phys., 275, 17
Li, G., Kong, X., Zank, G., & Chen, Y. 2013, ApJ, 769, 22
Li, Y. P., & Gan, W. Q. 2011, Sol. Phys., 269, 59
Lin, R. P., Dennis, B. R., Hurford, G. J., et al. 2002, Sol. Phys., 210, 3
Long, D. M., Harra, L. K., Matthews, S. A., et al. 2018, ApJ, 855, 74
Masuda, S., Kosugi, T., Hara, H., Tsuneta, S., & Ogawara, Y. 1994, Nature, 371, 495
Meegan, C., Lichti, G., Bhat, P. N., et al. 2009, ApJ, 702, 791
Minoshima, T., Yokoyama, T., & Mitani, N. 2008, ApJ, 673, 598
Müller, D., Marsden, R. G., St. Cyr, O. C., & Gilbert, H. R. 2013, Sol. Phys., 285, 25
Ning, H., Chen, Y., Wu, Z., et al. 2018, ApJ, 854, 178
Oka, M., Krucker, S., Hudson, H. S., & Saint- Hilaire, P. 2015, ApJ, 799, 129
Park, B. T., Petrosian, V., & Schwartz, R. A. 1997, ApJ, 489, 358
Parks, G. K., & Winckler, J. R. 1969, ApJ, 155, L117
Pesnell, W. D., Thompson, B. J., & Chamberlin, P. C. 2012, Sol. Phys., 275, 3
Share, G. H., Murphy, R. J., Skibo, J. G., et al. 2003, ApJ, 595, L85
Sharykin, I. N., & Kosovichev, A. G. 2018, ApJ, 864, 86
Shih, A. Y., Lin, R. P., & Smith, D. M. 2009, ApJ, 698, L152
Smith, D. M., Lin, R. P., Turin, P., et al. 2002, Sol. Phys., 210, 33
Sturrock, P. A. 1966, Nature, 211, 695
Sui, L., Holman, G. D., & Dennis, B. R. 2004, ApJ, 612, 546
Suri, A. N., Chupp, E. L., Forrest, D. J., & Reppin, C. 1975, Sol. Phys., 43, 415
Veronig, A. M., & Brown, J. C. 2004, ApJ, 603, L117
Warmuth, A., & Mann, G. 2016, A&A, 588, A115
White, S. M., Benz, A. O., Christe, S., et al. 2011, Space Sci. Rev., 159, 225
Yan, X. L., Yang, L. H., Xue, Z. K., et al. 2018, ApJ, 853, L18
Yang, S., Zhang, J., Zhu, X., & Song, Q. 2017, ApJ, 849, L21